

Electronic Supplementary Information (ESI) for

Anti-freezing Hydrogel Electrolyte with Regulated Hydrogen Bond Network Enables High-Rate and Long Cycling Zinc Batteries

*Shao-jie Guo,^a Meng-Yu Yan,^b Dong-Ming Xu,^a Pan He,^c Kai-Jian Yan,^b Jie-Xin Zhu,^b Yong-Kun Yu,^b Ze-Ya Peng,^a Yan-Zhu Luo,^{*a} and Fei-Fei Cao^{*a}*

a S. J. Guo, D. M. Xu, Z. Y. Peng, Prof. Y. Z. Luo, Prof. F. F. Cao
College of Chemistry, Huazhong Agricultural University,
Wuhan 430070, P.R. China
E-mail: caofeifei@mail.hzau.edu.cn; luoyanzhu@mail.hzau.edu.cn

b M. Y. Yan, K. J. Yan, J. X. Zhu, Y. K. Yu
State Key Laboratory of Advanced Technology for Materials Synthesis and Processing,
International School of Materials Science and Engineering,
Wuhan University of Technology,
Wuhan 430070, P.R. China

c P. He
Department of Chemistry, University College London,
London WC1H 0AJ, UK

Experimental section

Preparation of PAM-1,2-PG Hydrogel Electrolyte. A solution containing 1.035 g acrylamide (AM), 5 mL deionized (DI) water, 10 wt% 1,2-propanediol (1,2-PG), and 2 M zinc trifluoromethanesulfonate ($Zn(OTf)_2$) was prepared. Once AM had completely dissolved, 0.8 mg of N,N'-methylenebis(acrylamide) (MBA) was introduced. This resulting mixture was stirred overnight at room temperature. Subsequently, 5 mg of potassium persulfate (KPS) and 3.2 μ L of N,N,N',N'-Tetramethylethylenediamine (TMEDA) were added to the solution while maintaining vigorous stirring. After a 5-minute sonication to remove any bubbles, the mixture was poured into custom-made molds and then left at 35 °C for 4 hours to facilitate the formation of the hydrogel electrolyte (PAM-1,2-PG). The hydrogels thus obtained were stored at 4 °C in a refrigerator. For comparison, hydrogel electrolytes were also prepared using the same procedure: pure PAM hydrogel electrolyte with pure water solvent, hydrogel electrolyte with 10 wt% Gly cosolvent, and hydrogel electrolyte containing 10 wt% 1,3-PG cosolvent.

Synthesis of $VO_2 \cdot 0.4H_2O$ (VOH) cathode material. The VOH cathode material was synthesized using a hydrothermal method¹. Initially, 0.3638 g of V_2O_5 and 0.7564 g of $H_2C_2O_4$ were dissolved in 12 mL of deionized water and stirred at 75 °C for 2 hours until a clear blue solution was formed. After the precursor solution had cooled to room temperature, 3 mL of a 30 wt% H_2O_2 solution was added drop by drop and stirred for 20 minutes. Subsequently, 65 mL of ethanol was slowly introduced. The resultant precursor solution was then transferred into autoclaves, and the reaction was maintained at 180 °C for 100 minutes. After cooling to room temperature, the VOH cathode material was collected, washed thrice with 95% ethanol, and finally, the VOH powders were obtained by drying in a vacuum oven at 60 °C overnight.

Synthesis of FSC cathode material. The cottonseed hull residue underwent a series of treatments for its transformation². Initially, it was immersed in a 10 wt% dilute hydrochloric acid solution for a duration of 12 hours. Subsequently, the residue was

subjected to cleaning, drying, and calcination in an argon atmosphere at 500 °C for 1 hour, resulting in the formation of a precursor material. This precursor was then intimately mixed with KOH, with a mass ratio of KOH to biochar being 4. The mixture underwent further pyrolysis within a tubular furnace, carried out at 800 °C for 3 hours under a flowing Ar atmosphere, with a controlled heating rate of 3 °C per minute. Ultimately, the porous carbon product obtained was meticulously washed using dilute HCl to eliminate any residual KOH, followed by repeated washing with ultrapure water until the pH level reached 7. The product was then dried at 80 °C. This resulting carbon material was identified as FSC.

Characterizations. Various characterization techniques were employed to analyze the materials and their properties. Fourier-transform infrared spectroscopy (FTIR) and Raman spectroscopy (Horiba Lab RAM HR Evolution, with a laser wavelength of 532 nm) were used for structural assessment. The crystalline structures of the materials were examined using an X-ray diffractometer (Bruker D8 Advance X-ray diffractometer with filtered Cu K α radiation). Microscopic investigations were conducted through scanning electron microscopy (SEM, SU-8020). Proton nuclear magnetic resonance (^1H NMR) was performed on a Bruker Advance 600 MHz spectrometer in D $_2$ O. The viscosity of the electrolytes was measured through rotational rheometer (Kinexu) at room temperature. To ascertain the hydrogel electrolyte's freezing point, differential scanning calorimetry (DSC, TA Instruments) was employed. Mechanical properties were assessed using a universal tensile testing machine (Instron 5967, tensile rate 20 mm min $^{-1}$). The X-ray absorption near edge structure (XANES) and extended X-ray absorption fine structure (EXAFS) of Zn K-edge were recorded by transmission mode using the Japanese synchrotron radiation source (SPring-8). The Athena, Artemis and wavelet transform were used to extract and process EXAFS data according to standard procedures³. For the examination of Zn deposition surface topography after cycling, a laser scanning confocal microscope (LSCM, Zeiss LSM 800) was utilized. Furthermore, the interface morphologies of symmetric cells with zinc electrodes during Zn plating at 5 mA cm $^{-2}$ were observed via an optical microscope (YM710R,

YueScope) equipped with an HD camera. X-ray photoelectron spectroscopy (XPS) was performed using an ESCALAB 250Xi spectrometer with Al K α radiation (1486.6 eV). Time-of-flight secondary ion mass spectrometry (TOF-SIMS) analysis was carried out using a PHI Nano TOF 3 equipped with a Bi-cluster liquid metal ion gun (LMIG).

Electrochemical Measurements. The construction of CR2032 cells involved sandwiching various hydrogel electrolytes between two electrodes, with all the hydrogel electrolytes being cut into 16 mm diameter discs. Electrochemical assessments were conducted utilizing an electrochemical workstation (CHI760E, Chenhua Instruments, China). Linear scanning voltammetry (LSV) and ion conductivity (σ) measurements were performed by placing the electrolyte between two stainless steel components. LSV measurements were executed at a scan rate of 0.01 V s⁻¹ within a voltage range of 0~3 V. The calculation of ionic conductivity for hydrogel electrolytes followed the equation denoted as S1:

$$\sigma = \frac{l}{R \cdot A} \quad (\text{S1})$$

Where l , R and A are the thickness, the resistance and area the of electrolyte, respectively. The electrochemical impedance spectroscopy (EIS) was measured in the frequency range from 10⁵ to 10⁻¹ Hz by assembling Zn||Zn symmetric batteries. The activation energy (E_a) was further obtained from the temperature-dependent EIS curves according to the Arrhenius equation S2:

$$\frac{1}{R_{ct}} = A_0 \exp\left(-\frac{E_a}{RT}\right) \quad (\text{S2})$$

where R_{ct} , A_0 , E_a , R and T represent the interfacial resistance, pre-exponential factor, activation energy, molar gas constant, and Kelvin temperature, respectively.

The cycling performance of both Zn||Zn symmetric cells and Zn||Cu asymmetric cells was assessed using a Neware battery tester. Charge-discharge experiments were conducted at low temperatures (-30 °C) utilizing a LAND battery test system equipped

with a high and low-temperature test chamber (CTE-SE7506-05F, China-Scicooling (Beijing) Science Technology Co., LTD.).

For the preparation of the VOH cathode, VOH powder, Ketjen black EC-600JD carbon (KB), and polytetrafluoroethylene (PTFE) binder were mixed in a mass ratio of 7:2:1 and homogenized in 2-propanol at room temperature to form a uniform paste. This paste was then rolled into a thin film and cut into the desired shape. The resulting composite materials were pressed onto Ti mesh and dried at 60 °C in an oven overnight, yielding the final VOH cathode. The Zn||VOH cells underwent galvanostatic charge/discharge cycles within the voltage range of 0.2 ~ 1.4 V vs. Zn²⁺/Zn. The average mass loading of the active material VO₂ in the coin cell is approximately 1.4 mg cm⁻², while in the pouch cell it is about 3.3 mg cm⁻². For the assembly of Zn||VOH full cells with a low N/P ratio of 3.5, the mass loading of the active material is increased to 7.8 mg cm⁻².

To prepare the FSC electrodes, a mixture containing 80 wt% FSC powders, 10 wt% KB, and 10 wt% PTFE was processed following the same methodology as the VOH cathode. These materials were then pressed onto Ti mesh. The Zn||FSC cells were subjected to galvanostatic charge/discharge cycles within the voltage range of 0.2 ~ 1.8 V vs. Zn²⁺/Zn. The average mass loading of FSC active material is about 1.0 mg cm⁻².

Device fabrication. Assembly of pouch cell. The flexible battery assembly was conducted in ambient conditions. Initially, the Zn foil (~100 μm thickness) underwent a pretreatment process involving polishing with 2000 and 3000 mesh sandpaper and was subsequently cut into specific rectangular shapes. The cathode electrodes, differing in size, were prepared following the previously outlined procedure. Sections of the PAM-1,2-PG hydrogel electrolyte were cut into the desired dimensions. Pouch cells were fabricated by interleaving the PAM-1,2-PG hydrogel electrolyte between Zn foils and VOH cathodes, followed by sealing with aluminum-plastic films at a temperature of 180°C.

Preparation of flexible devices. The zinc foil, post-pretreatment, was cut into dimensions of either 10×25 mm or 20×20 mm. Two VOH cathodes of uniform size

(7×23 mm or 18×18 mm) were pressed onto both sides of a Ti mesh (10×25 mm or 20×20 mm). Subsequently, pouch cells were assembled by stacking in the following order: Zn-(PAM-1,2-PG)-VOH-(PAM-1,2-PG)-Zn, and were then sealed using polyethylene films. Finally, five pouch cells were interconnected in series to fabricate flexible devices.

Computational Methods. Binding energy and adsorption energy calculation. The theoretical calculations were performed via the Gaussian 16 suite of program⁴. The structures of the studied molecules (denoted by M1~M4) and their dimers for binding energy calculation were fully optimized at the B3LYP-D3BJ/TZVP level of theory. The PBE0 functional was adopted for adsorption energy calculations in combination with the Grimme's D3(BJ) dispersion correction. For geometry optimization and frequency calculations, the def2-SVP basis set was used for all atoms. The polarizable continuum model (PCM) implicit solvation model was used to account for the water solvation effect at same time. The solvent effect (H₂O) was included in the calculations using the solvation model based on the density (SMD) model. The vibrational frequencies of the optimized structures were carried out at the same level. The structures were characterized as a local energy minimum on the potential energy surface by verifying that all the vibrational frequencies were real. The binding energy (ΔE) of the optimized cluster was calculated at the B3LYP-D3BJ/def2-TZVP level of theory. ΔE is defined as the difference between the complex and the sum of energies of monomers, which can be obtained by the following formulas $\Delta E = E(\text{M-dimer}) - 2 * E(\text{M})$.

Molecular dynamics simulation. Molecular dynamics (MD) simulations of blank and experimental electrolyte systems were performed using GROMACS 2021.5 package with OPLS-AA force field.^{5, 6} Blank electrolyte system (PAM) was packed with 100 PAM, 11200 H₂O and 400 Zn(OTf)₂, and experimental system (PAM-1,2-PG) was packed with 100 PAM, 11200 H₂O, 300 PG and 400 Zn(OTf)₂. The force field parameters of OTf⁻ were obtained from the literature and a charge scaling of 0.8 for Zn²⁺ and OTf⁻ were adopted to mimic polarization and charge transfer effects.^{7, 8} The force field parameters of PG and PAM (n=6) were generated using LigParGen web

server and its 1.2-scaling CM5 charges were based on DFT calculation with B3LYP/def2-SVP level with DFT-D3 dispersion correction and SMD (water) implicit solvation model by Gaussian program and wavefunction analysis by Multiwfn.^{9, 10} Energy minimization was performed by using the steepest descent algorithm with a force tolerance of 500 kJ mol⁻¹ nm⁻¹. In all the three directions, periodic boundary conditions were imposed. Then these systems were relaxed for 1 ns under NPT ensemble and box size eventually stabilized at 7.8×7.8×7.8 and 8.0×8.0×8.0 nm³ for blank and experimental system, respectively.

After completing the above steps, 50 ns NPT MD simulations were performed. Pressure was maintained at 1 bar by the Parrinello-Rahman barostat in an isotropic manner and temperature was maintained at 298 K by the V-rescale thermostat.^{11, 12} Lennard-Jones interactions were calculated within a cutoff of 1.2 nm, and electrostatic interactions beyond 1.2 nm were treated with particle-mesh Ewald (PME) method with a grid spacing of 0.16 nm. UCSF ChimeraX was used to visualize all simulation results.¹³

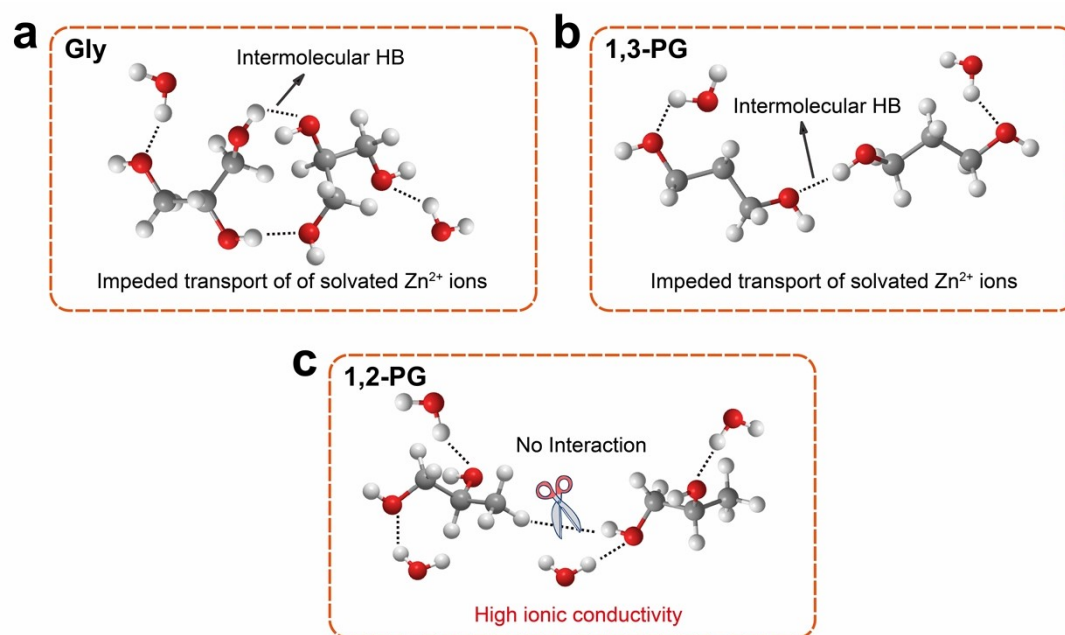


Figure S1. Schematic illustration of intermolecular force of solvent-solvent. (a) glycerol (Gly) system, (b) 1,3-propanediol (1,3-PG) system, and (c) 1,2-propanediol (1,2-PG) system.

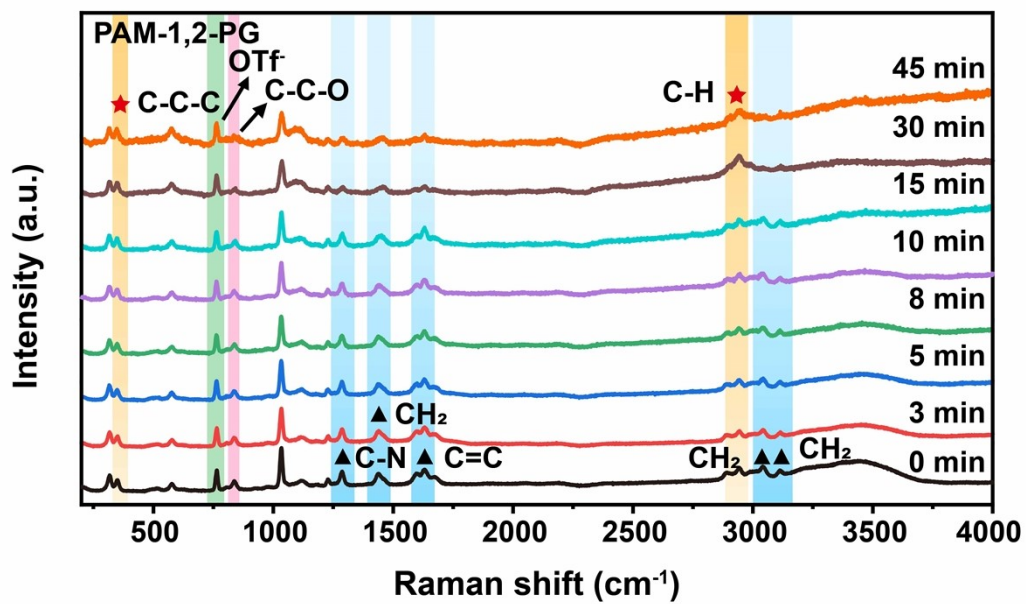


Figure S2. The *in-situ* Raman spectrum of PAM-1,2-PG under different reaction times.

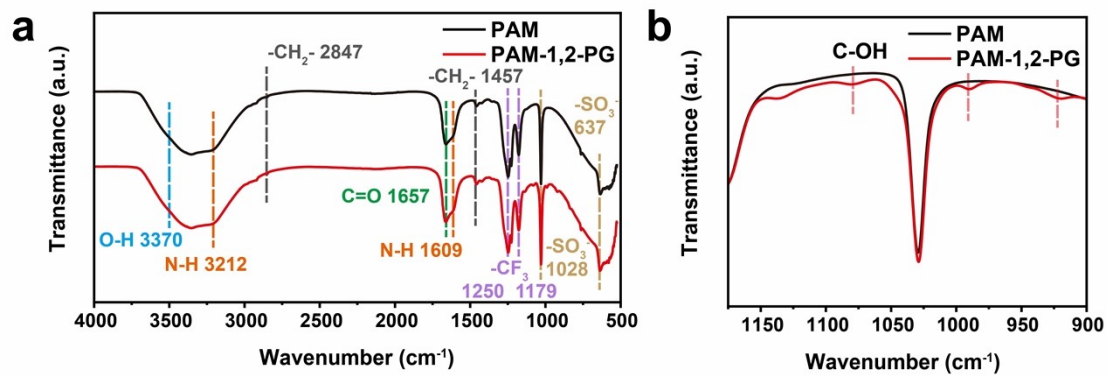


Figure S3. FTIR spectra of PAM and PAM-1,2-PG hydrogel electrolytes in the range of (a) 500-4000 cm^{-1} and (b) 900-1175 cm^{-1} (1,2-PG characteristic peaks).

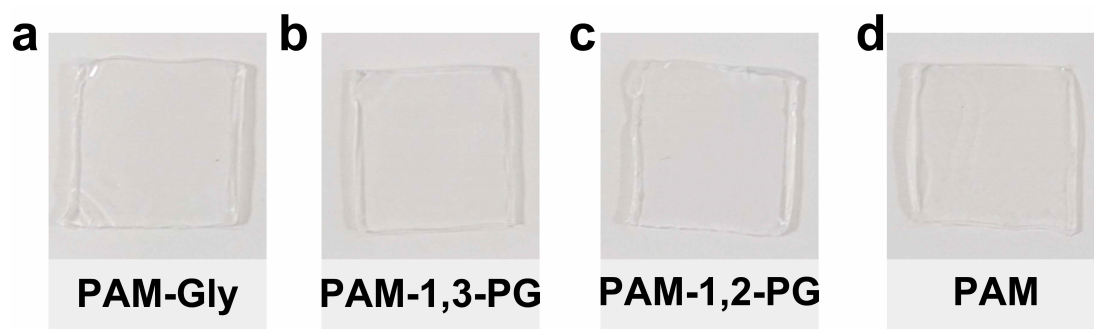


Figure S4. Optical photos of (a) PAM-Gly, (b) PAM-1,3-PG, (c) PAM-1,2-PG, and (d) PAM hydrogel electrolytes.

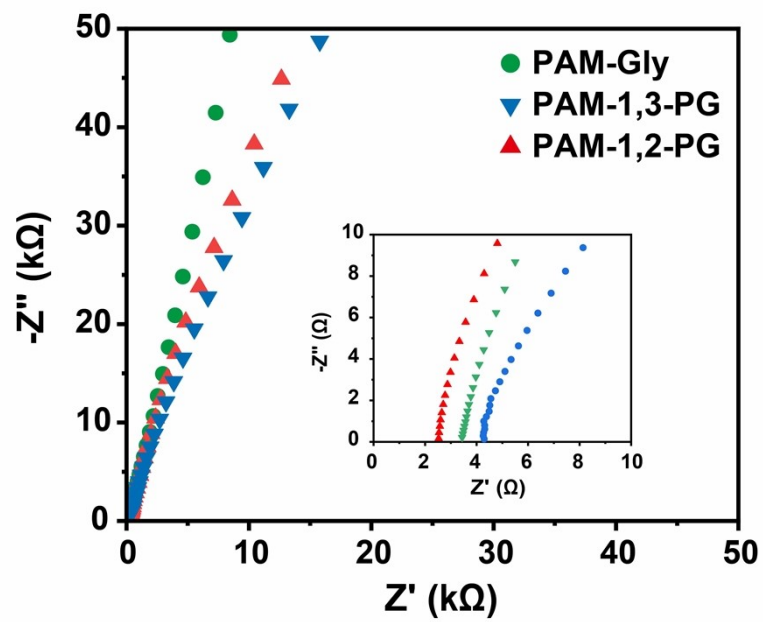


Figure S5. EIS spectra of different hydrogel electrolytes in the frequency range from 100 kHz to 0.01 Hz.

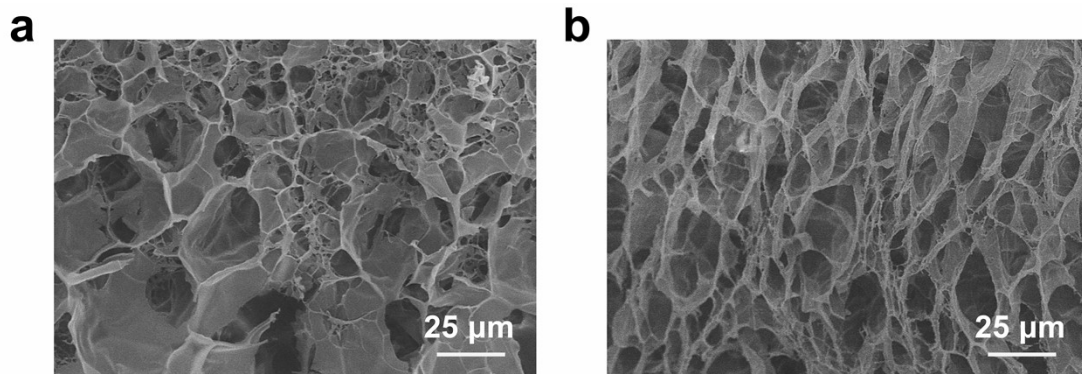


Figure S6. The SEM image of the freeze-dried (a) PAM and (b) PAM-1,2-PG hydrogel electrolytes.

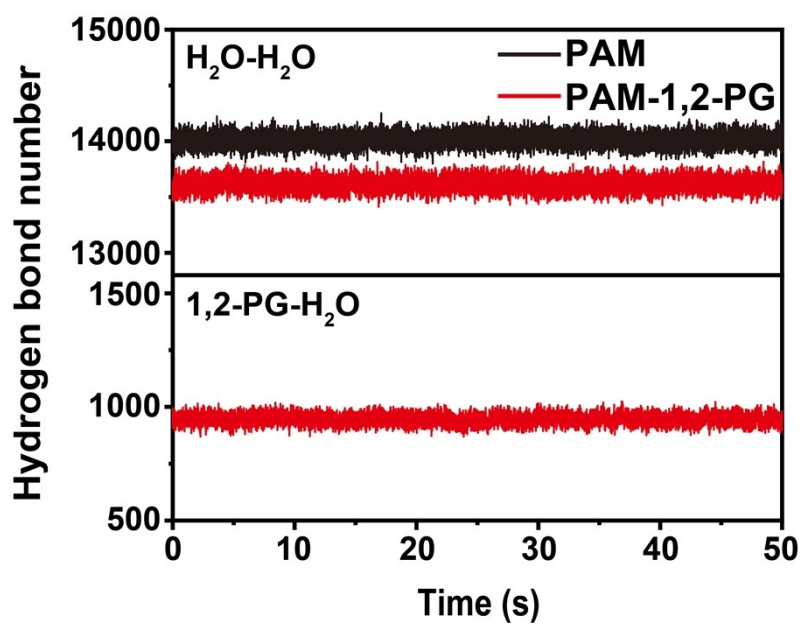


Figure S7. Number counts for H₂O-H₂O hydrogen bonds inside PAM electrolyte and H₂O-H₂O and 1,2-PG-H₂O hydrogen bonds inside PAM-1,2-PG electrolyte obtained by MD simulation.

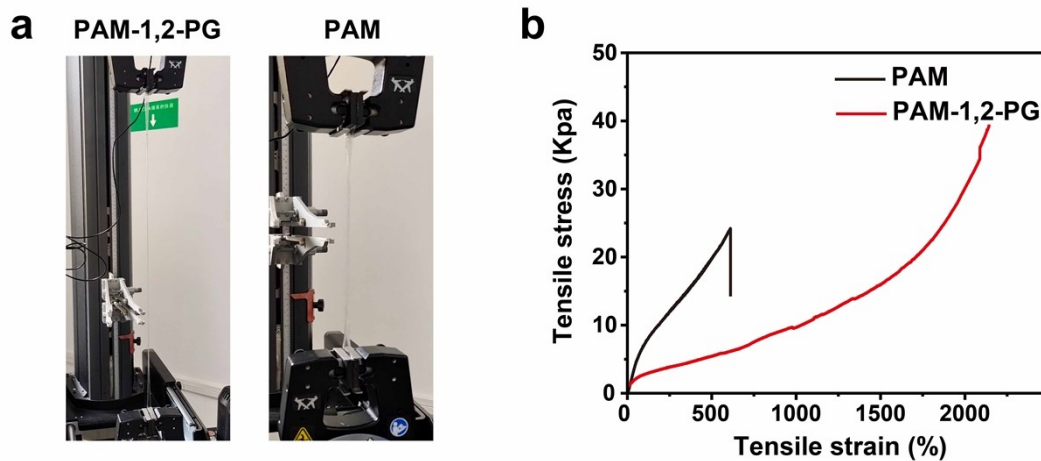


Figure S8. (a) Tensile mechanical properties test. (b) Tensile stress-strain curves of PAM, PAM-Gly, PAM-1,2-PG and PAM-1,3-PG.

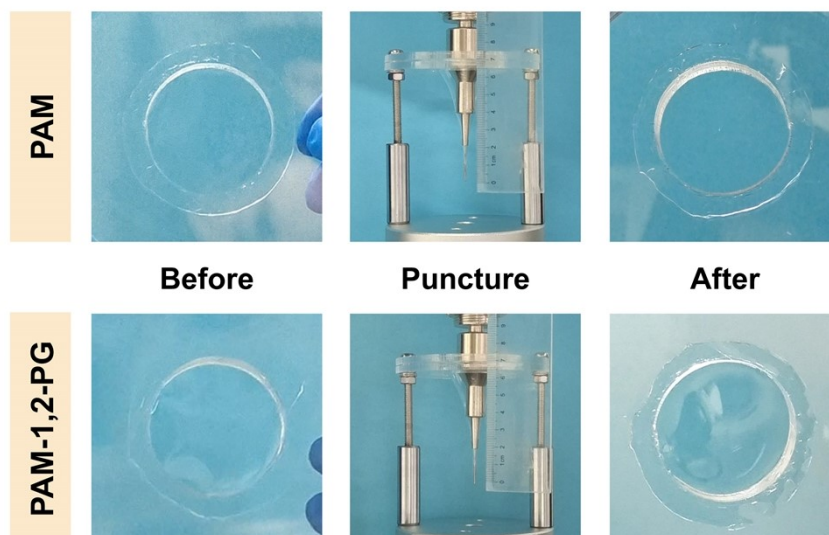


Figure S9. The digital photos of PAM and PAM-1,2-PG hydrogel electrolytes before, under, and after puncture (a vertically oriented puncture needle with a diameter of 2 mm).

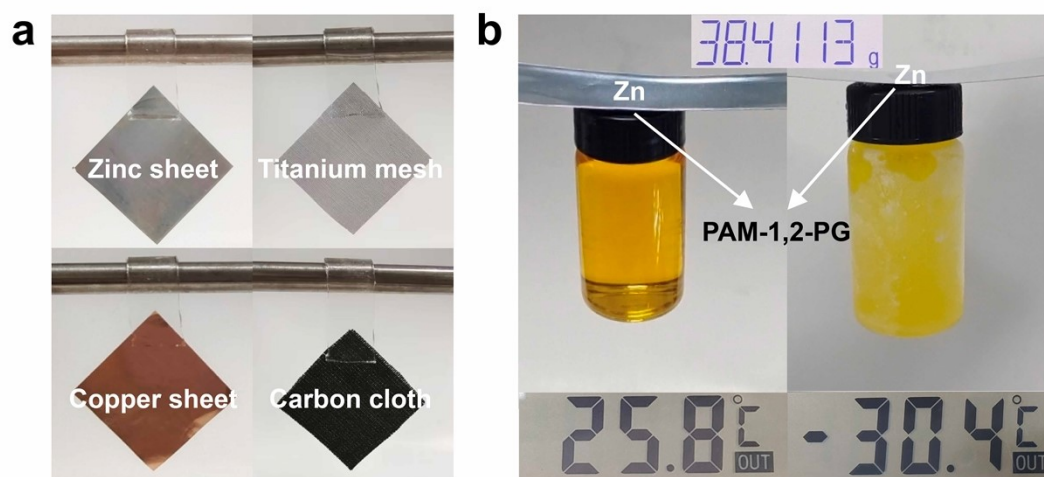


Figure S10. (a) Photos demonstrate the satisfactory interfacial adhesion of PAM-1,2-PG hydrogel on various substrates (e.g., zinc sheet, titanium mesh, copper sheet, and carbon paper). (b) Photos shows the adhesion of PAM-1,2-PG hydrogel electrolyte to zinc sheet at room temperature and low temperature.

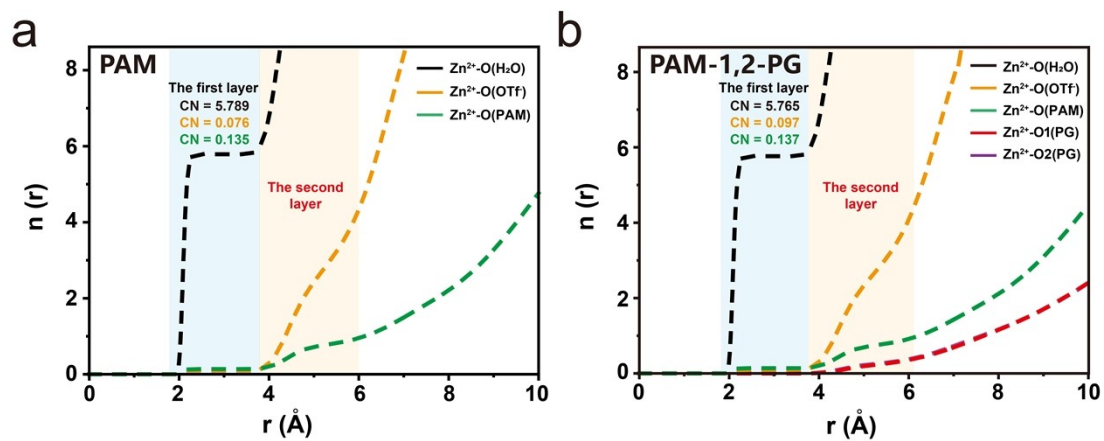


Figure S11. The CN of oxygen atom in molecules around Zn^{2+} by MD simulations in (c) PAM and (d) PAM-1,2-PG hydrogel electrolytes.

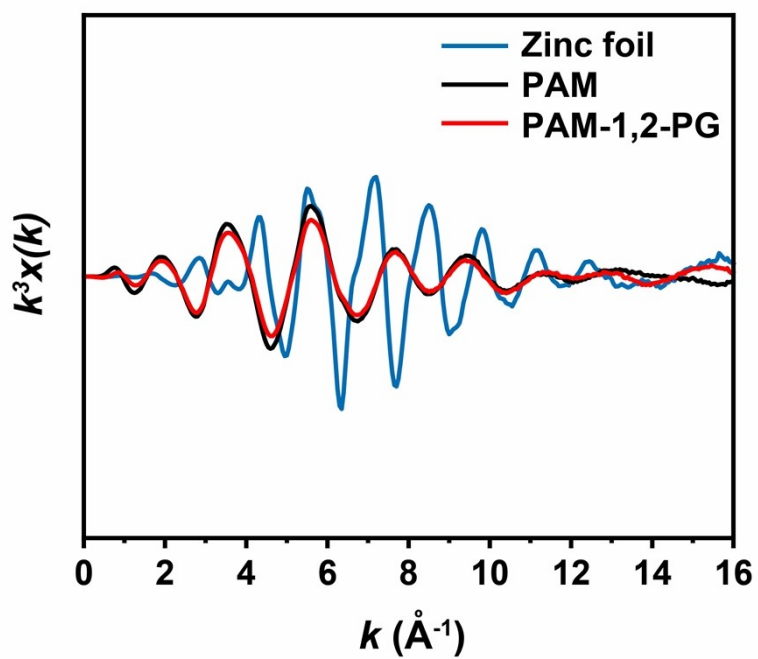


Figure S12. k^3 -weighted Fourier transform of Zn K-edge EXAFS spectra in the k -space of the Zn foil, PAM and PAM-1,2-PG hydrogel electrolytes.

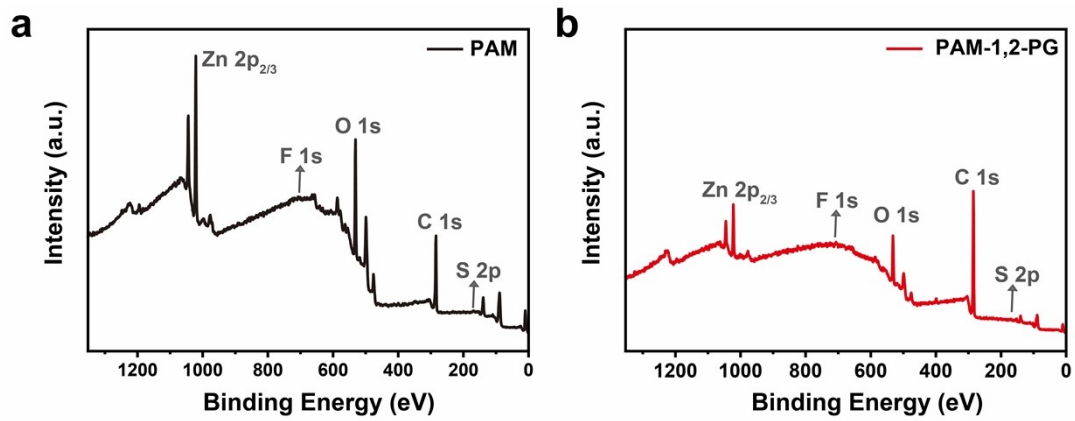


Figure S13. Total XPS spectra of Zn anode after the contact with PAM (a) and PAM-1,2-PG (b) hydrogel electrolytes for 14 h.

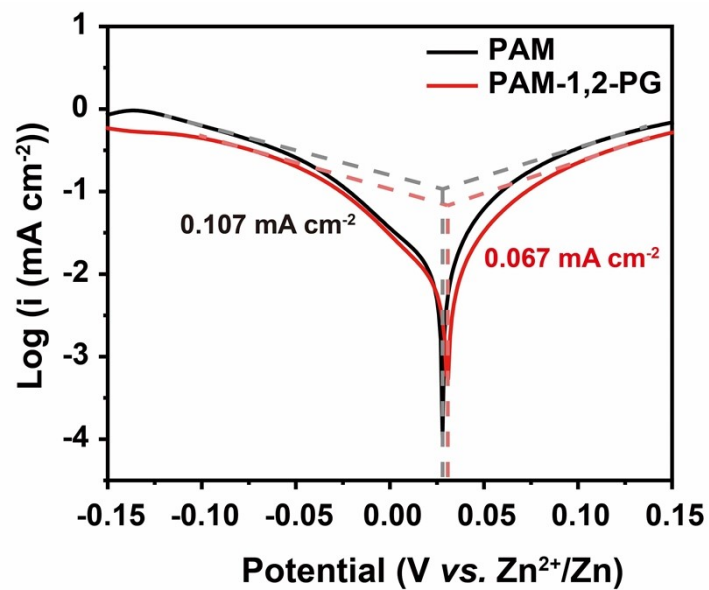


Figure S14. Tafel curves of the Zn||Zn symmetric cells assembled with PAM and PAM-1,2-PG hydrogel electrolytes.

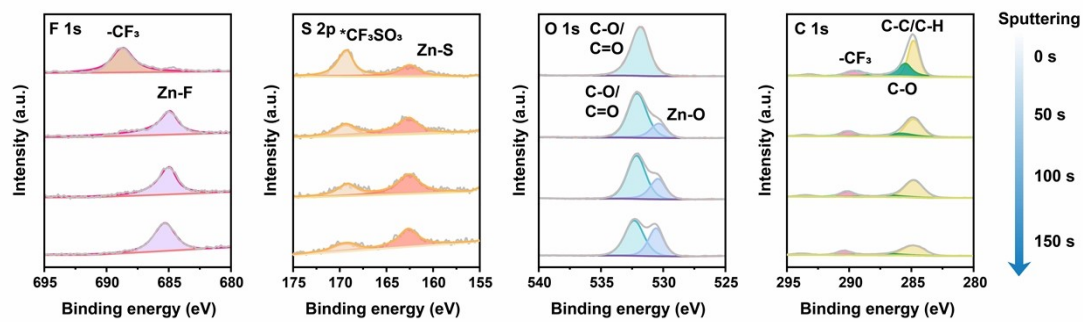


Figure S15. F 1s, S 2p, O 1s, and C 1s XPS spectra of the Zn electrode surface with PAM hydrogel electrolyte after cycling at different Ar^+ etching times.

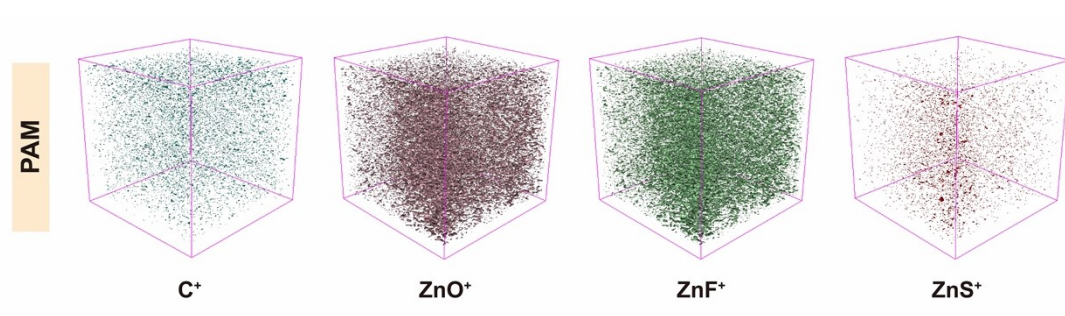


Figure S16. 3D reconstruction maps of Zn electrodes retrieved from PAM hydrogel electrolyte measured by TOF-SIMS.

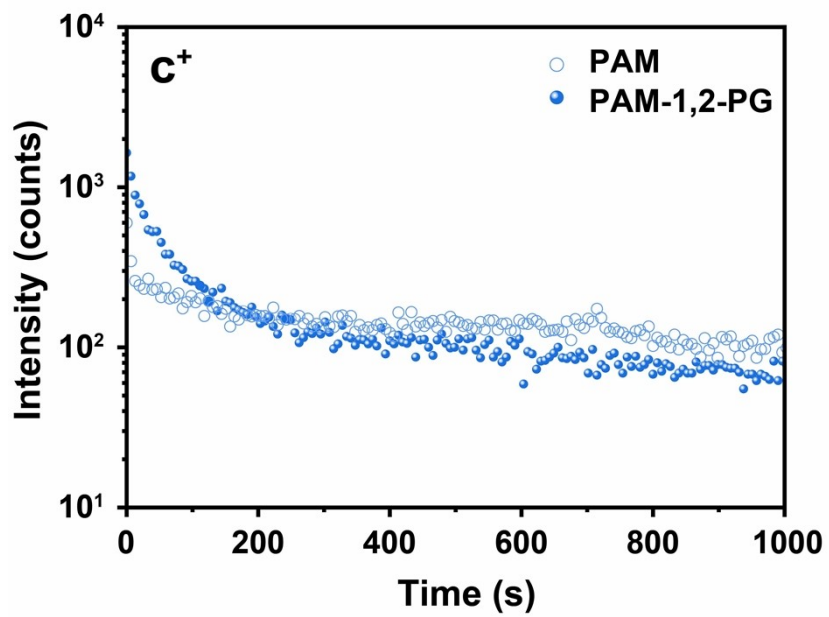


Figure S17 Depth intensity profile of C^+ on the cycled Zn surface measured by TOF-SIMS.

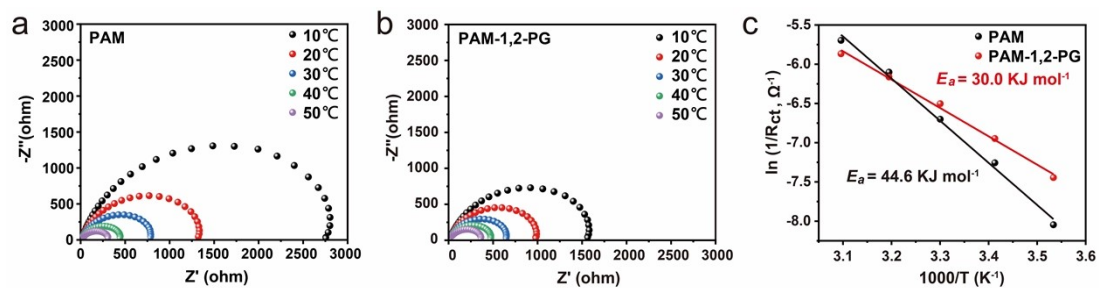


Figure S18. The Nyquist curves of Zn||Zn symmetric cells with (a) PAM and (b) PAM-1,2-PG hydrogel electrolytes at different temperatures. (c) Arrhenius plots and the corresponding activation energies obtained in PAM and PAM-1,2-PG.

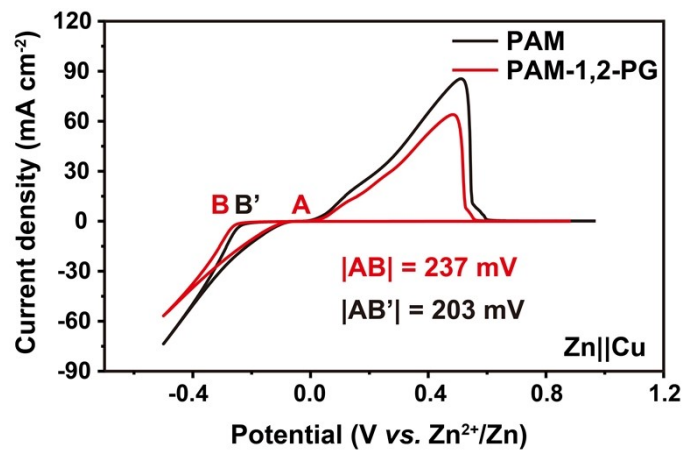


Figure S19. CV curves of Zn||Cu asymmetric cells using PAM and PAM-1,2-PG hydrogel electrolytes.

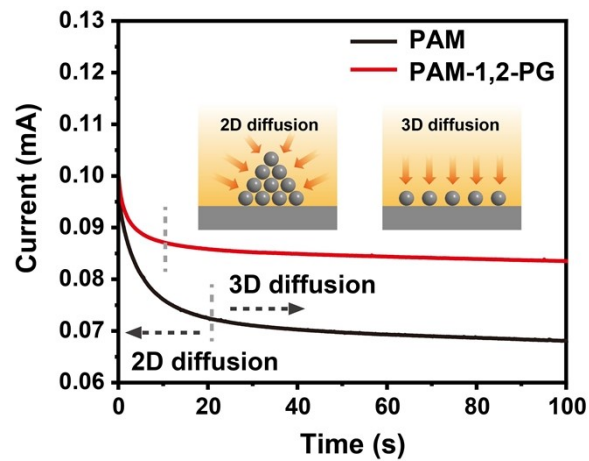


Figure S20. Chronoamperometric curves of symmetrical cells based on PAM and PAM-1,2-PG with a polarization voltage of 50 mV.

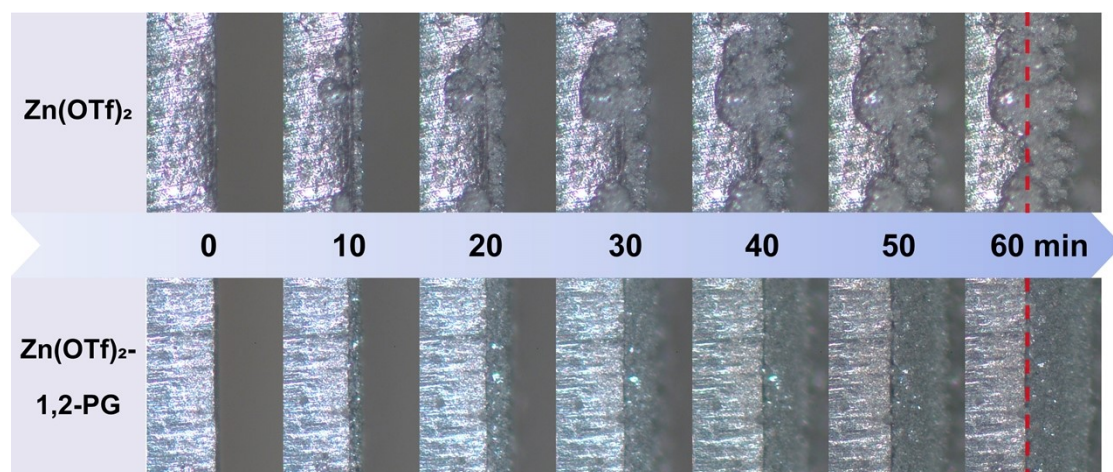


Figure S21. *In-situ* optical images of the Zn deposition in Zn||Zn symmetric cells with $\text{Zn}(\text{OTf})_2$ and $\text{Zn}(\text{OTf})_2$ -1,2-PG liquid electrolyte (deposition time of 60 minutes at 5 mA cm^{-2}).

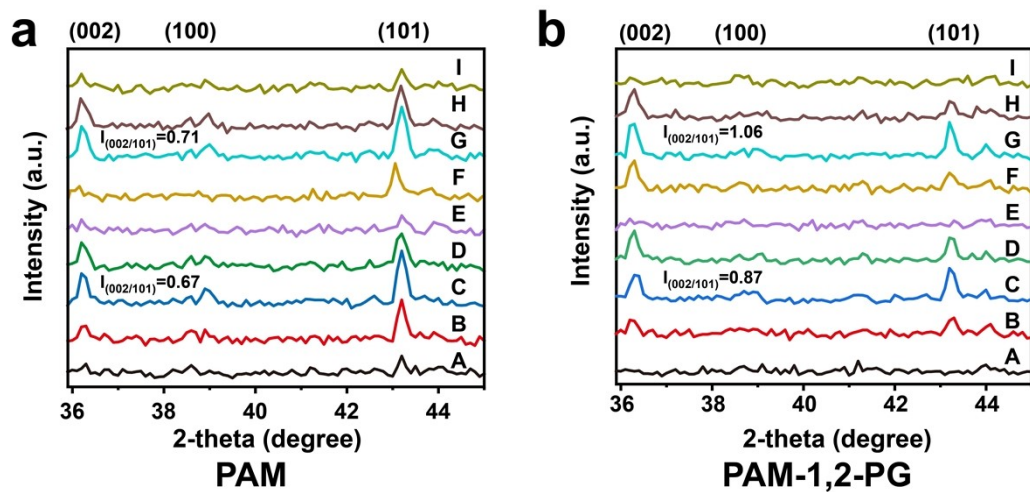


Figure S22. The *in-situ* XRD patterns of (a) PAM and (b) PAM-1,2-PG hydrogel electrolytes.

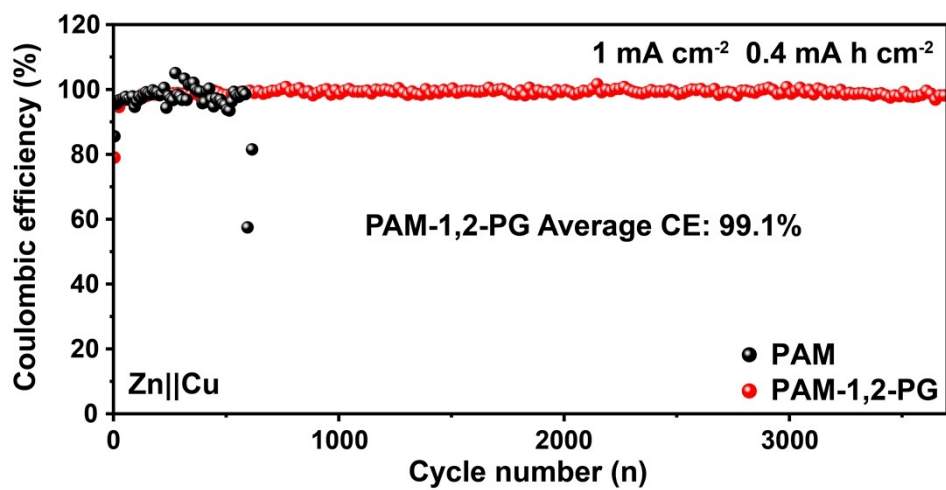


Figure S23. CEs of Zn||PAM||Cu and Zn||PAM-1,2-PG||Cu cells at 1 mA cm^{-2} with a cut-off voltage of 1 V.

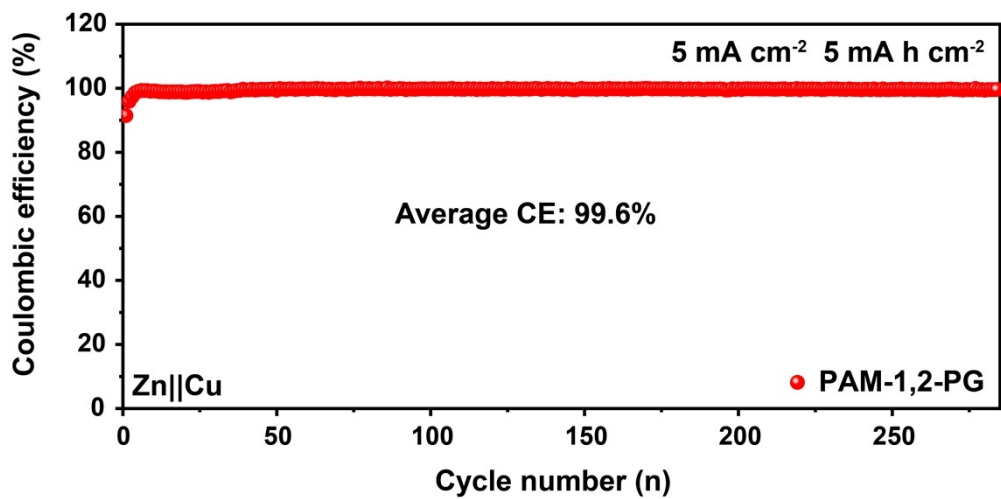


Figure S24. CEs of Zn||PAM-1,2-PG||Cu cells at 5 mA cm⁻² and 5 mA h cm⁻² with a cut-off voltage of 1 V.

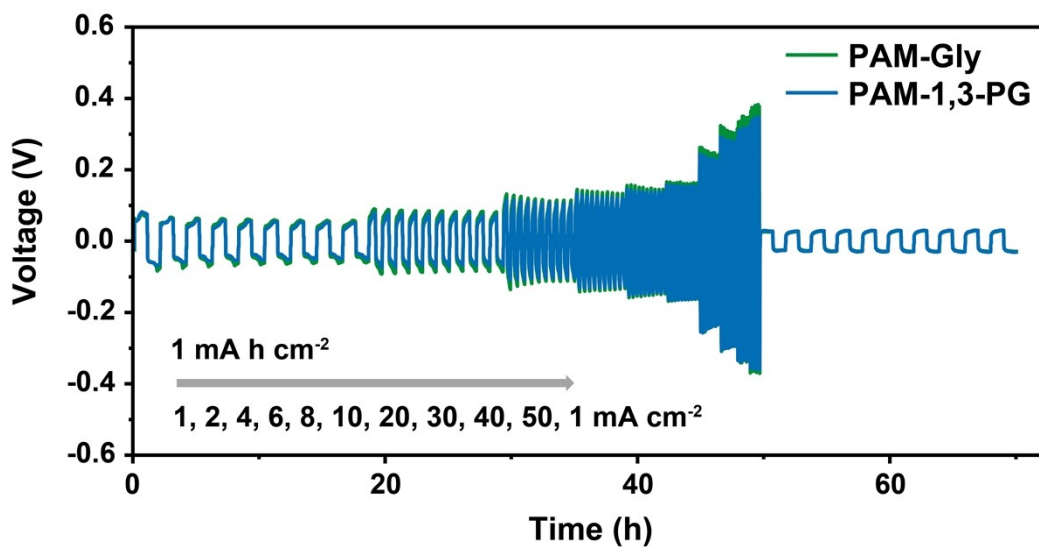


Figure S25. Rate performance of the Zn||Zn symmetric cells based on the PAM-Gly and PAM-1,3-PG gel electrolytes from 1 to 50 mA cm⁻².

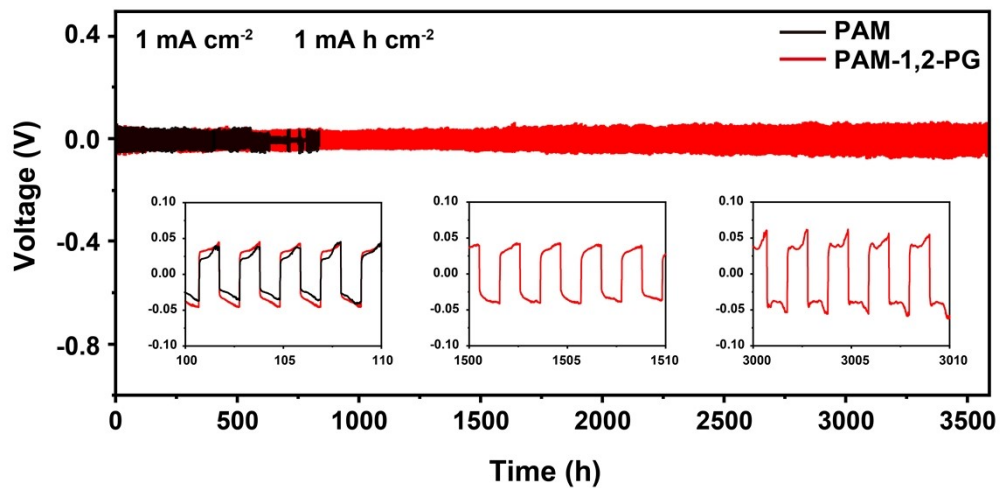


Figure S26. Cycling performance of Zn||Zn symmetric cells using PAM and PAM-1,2-PG hydrogel electrolytes at 1 mA cm^{-2} and 1 mA h cm^{-2} .

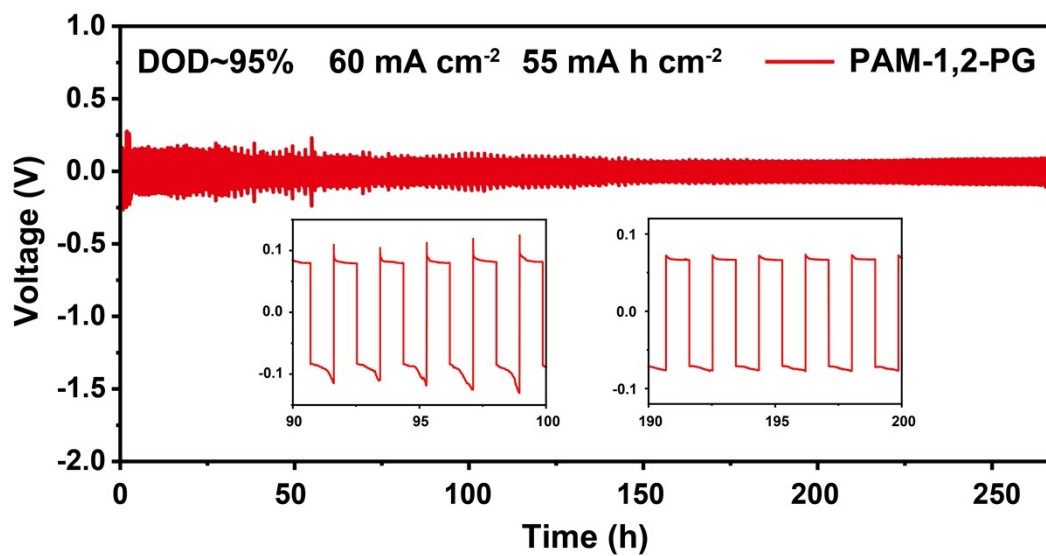


Figure S27. Electrochemical performance of Zn||Zn symmetric cells with PAM-1,2-PG hydrogel electrolyte at 60 mA cm⁻² and 55 mA h cm⁻² with a high DOD of 95%.

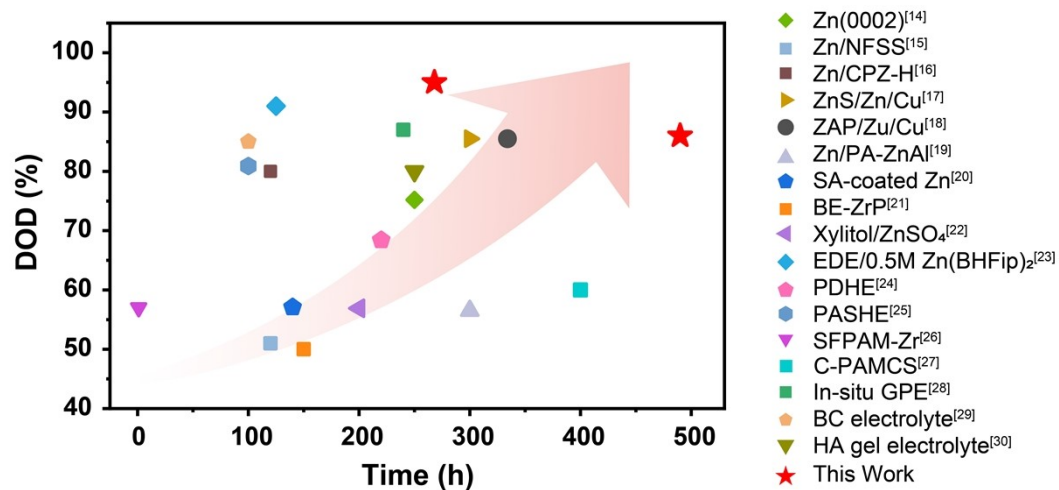


Figure S28. Comparisons of the DOD and cycling duration between this work and recent reported literatures.¹⁴⁻³⁰

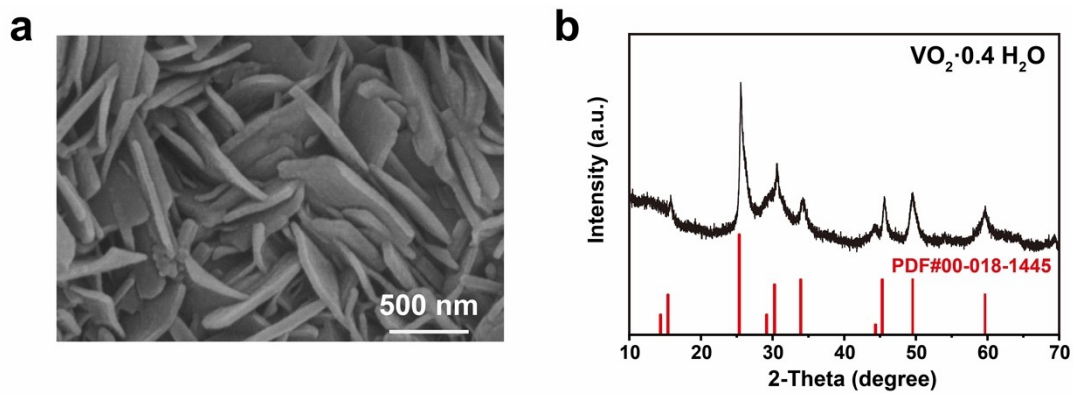


Figure S29. The SEM image (a) and XRD spectrum (b) of $\text{VO}_2 \cdot 0.4 \text{H}_2\text{O}$ (VOH).

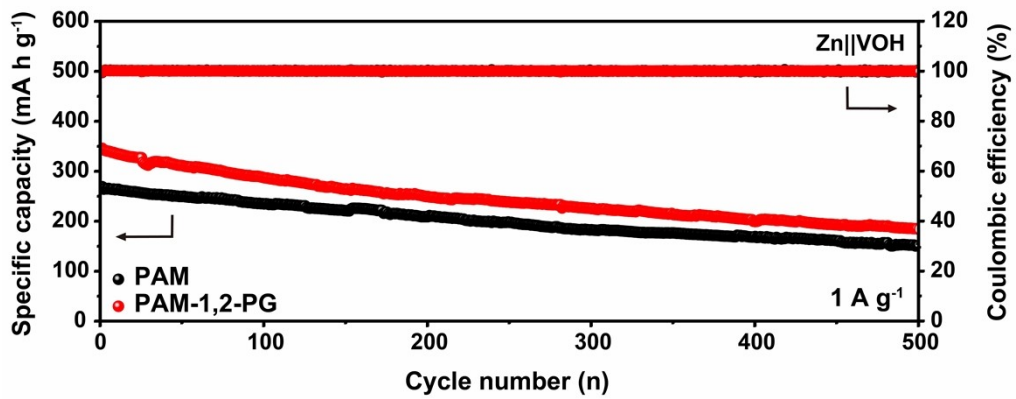


Figure S30. Cycling performance of the AZIBs full cells with PAM and PAM-1,2-PG hydrogel electrolytes at room temperature.

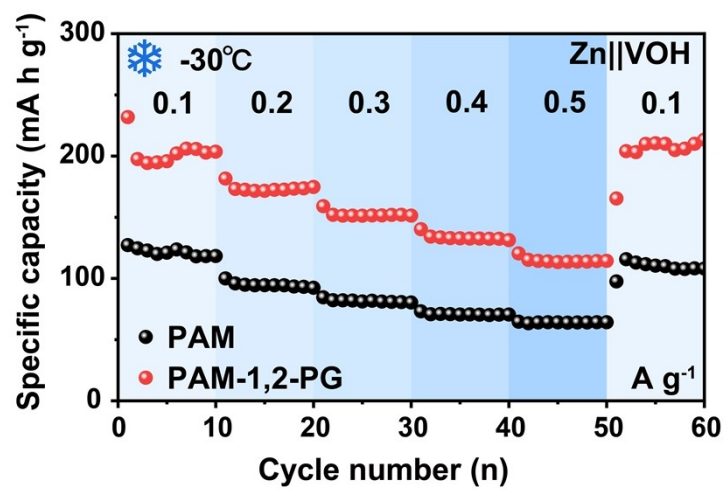


Figure S31. The SEM image (a) and XRD spectrum (b) of VO₂·0.4 H₂O (VOH).

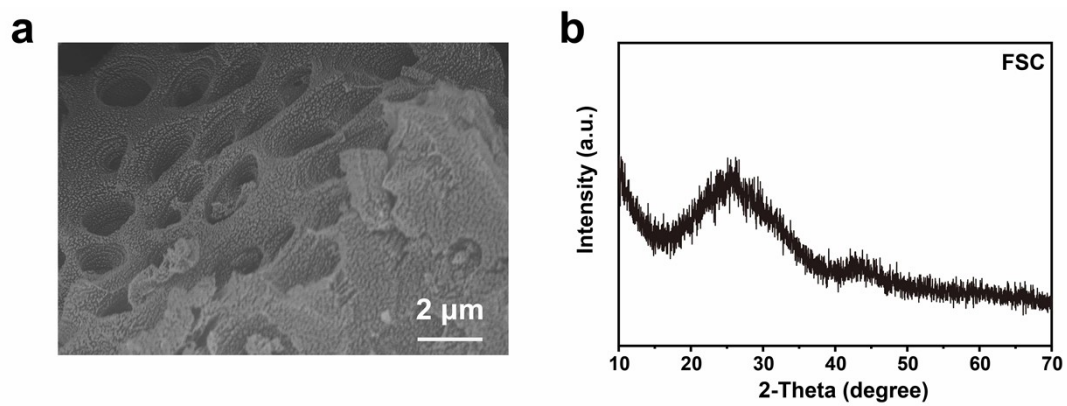


Figure S32. (a) The SEM image of FSC. (b) The XRD pattern of FSC.

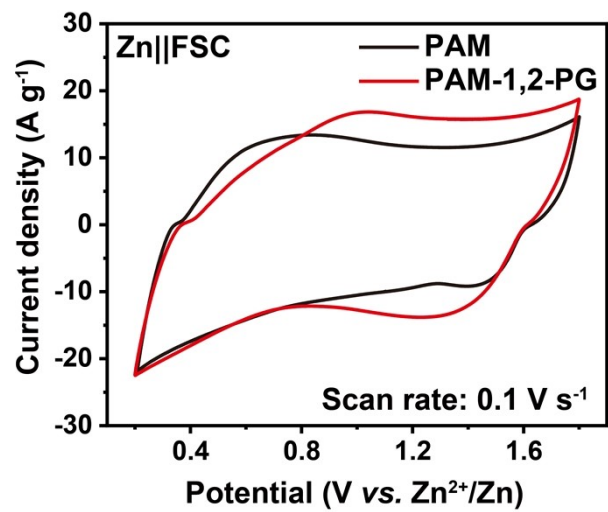


Figure S33. CV curves of Zn||FSC AZICs at 0.1 V s⁻¹.

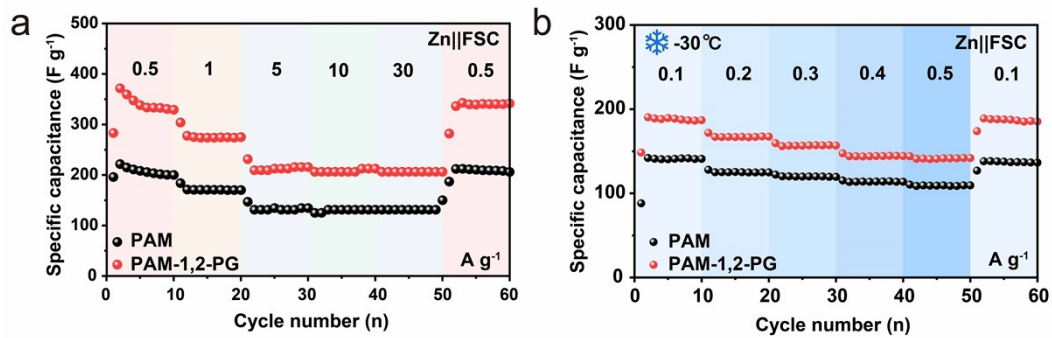


Figure S34. Rate performance of the Zn||FSC AZICs with PAM and PAM-1,2-PG hydrogel electrolytes at (a) room temperature and (b) -30°C.

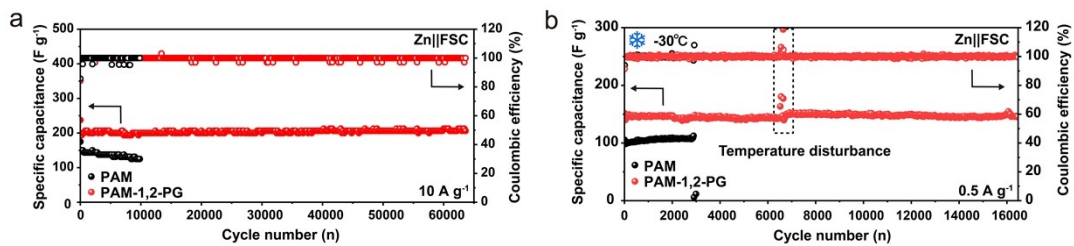


Figure S35. Cycling performance of the AZICs at (a) room temperature and (b) -30 °C.

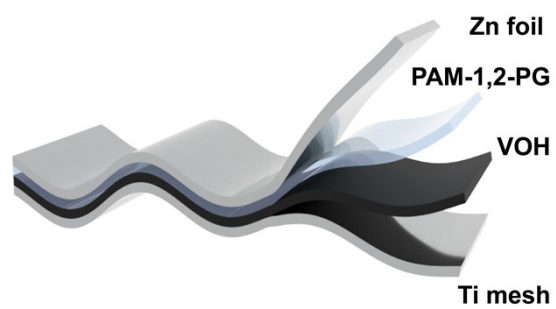


Figure S36. Schematic illustrations of the flexible Zn||VOH pouch cell.

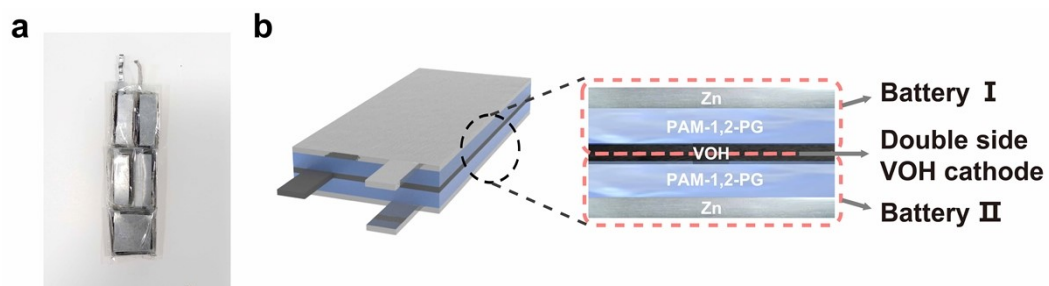


Figure S37. (a) The photo shows the structure of the battery inside the watch. (b) Detailed illustration of a bi-cell structure inside a pouch cell.

Table S1. Comparison of cumulative capacities for Zn||Zn symmetrical cells between this work and previous reports with various strategies.

Defined name	Current density (mA cm ⁻²)	Areal capacity (mA h cm ⁻²)	Lifespan (h)	Cumulative capacity (mA h cm ⁻²)	References
Zn/NTP	20	5	125	1250	<i>Adv. Mater.</i> , 2022, 34 , 2206239
Zn/SHn	10	5	1000	5000	<i>Adv. Mater.</i> , 2022, 34 , 2202382
HDES	1	1	4500	2250	<i>Energy Environ. Sci.</i> , 2023, 16 , 2540
Zn(BBI) ₂	20	1	700	7000	<i>Adv. Mater.</i> , 2023, 35 , 2210055
2-Propanol	15	15	500	3750	<i>Adv. Mater.</i> , 2022, 34 , 2207344
ZnSO ₄ -xylitol	5	1	1000	2500	<i>Angew. Chem. Int. Ed.</i> , 2023, 62 , e202218872
ZnSO ₄ -Bet	0.5	0.5	4200	1050	<i>Adv. Mater.</i> , 2022, 35 , 2208237
C-PAMCS	10	10	1500	7500	<i>Adv. Mater.</i> , 2023, 35 , 2300498
CP/EGZn/Betaine	0.5	0.5	2000	500	<i>Energy Environ., Sci.</i> 2023, 16 , 1291
PAM/PPF-SSEs	2	4	2000	2000	<i>Nat. Commun.</i> , 2023, 14 , 2925
PCZ-gel	20	20	700	7000	<i>Angew. Chem. Int. Ed.</i> , 2023, 135 , e202217833
PASHE	20	1	200	2000	<i>Adv. Energy Mater.</i> , 2022, 12 , 2202219
In situ GPE	1	1	5100	2550	<i>Adv. Mater.</i> , 2022, 34 , 2207118
PMC	1	1	5000	2500	<i>Energy Storage Mater.</i> , 2022, 49 , 172
CSAM-C	3	3	500	750	<i>Adv. Mater.</i> , 2022, 34 , 2110140
PDZ-H	5	10	800	2000	<i>Adv. Funct. Mater.</i> , 2022, 32 , 2112540
CT3G30	2	2	800	800	<i>Adv. Mater.</i> , 2021, 33 , e2007559
PAM-1,2-PG	10	1	2160	10800	This Work
	100	50	490	24500	

Reference

- 1 Y. Tao, D. Huang, H. Chen, Y. Luo, *ACS Appl. Mater. Interfaces*, 2021, **13**, 16576.
- 2 P. Wang, H. Ye, Y. Yin, H. Chen, Y. Bian, Z. Wang, F. Cao, Y. Guo, *Adv. Mater.*, 2019, **31**, 1805134.
- 3 B. Ravel, M. Newville, *J. Synchrotron Rad.*, 2005, **12**, 537.
- 4 M. J. F. Revision A.03, G. W. Trucks, H. B. Schlegel, G. E. Scuseria, M. A. Robb, J. R. Cheeseman, G. Scalmani, V. Barone, G. A. Petersson, H. Nakatsuji, X. Li, M. Caricato, A. V. Marenich, J. Bloino, B. G. Janesko, R. Gomperts, B. Mennucci, H. P. Hratchian, J. V. Ortiz, A. F. Izmaylov, J. L. Sonnenberg, D. Williams-Young, F. Ding, F. Lipparini, F. Egidi, J. Goings, B. Peng, A. Petrone, T. Henderson, D. Ranasinghe, V. G. Zakrzewski, J. Gao, N. Rega, G. Zheng, W. Liang, M. Hada, M. Ehara, K. Toyota, R. Fukuda, J. Hasegawa, M. Ishida, T. Nakajima, Y. Honda, O. Kitao, H. Nakai, T. Vreven, K. Throssell, J. A. Montgomery, Jr., J. E. Peralta, F. Ogliaro, M. J. Bearpark, J. J. Heyd, E. N. Brothers, K. N. Kudin, V. N. Staroverov, T. A. Keith, R. Kobayashi, J. Normand, K. Raghavachari, A. P. Rendell, J. C. Burant, S. S. Iyengar, J. Tomasi, M. Cossi, J. M. Millam, M. Klene, C. Adamo, R. Cammi, J. W. Ochterski, R. L. Martin, K. Morokuma, O. Farkas, J. B. Foresman, D. J. Fox, *Gaussian 16 Revision. A.03*, Gaussian Inc., Wallingford, CT, 2016.
- 5 G. A. Kaminski, R. A. Friesner, J. Tirado-Rives, W. L. Jorgensen, *J. Phys. Chem. B*, 2001, **105**, 6474.
- 6 M. J. Abraham, T. Murtola, R. Schulz, S. Páll, J. C. Smith, B. Hess, E. Lindahl, *SoftwareX*, 2015, **1**, 19.
- 7 B. Doherty, X. Zhong, S. Gathiaka, B. Li, O. Acevedo, *J. Chem. Theory Comput.*, 2017, **13**, 6131.
- 8 S. V. Sambasivarao, O. Acevedo, *J. Chem. Theory Comput.*, 2009, **5**, 1038.
- 9 T. Lu, F. Chen, *J. Comput. Chem.*, 2012, **33**, 580.
- 10 L. S. Dodda, I. Cabeza de Vaca, J. Tirado-Rives, W. L. Jorgensen, *Nucleic Acids Res.*, 2017, **45**, W331.
- 11 Bussi G, Donadio D, P. M., *J. Chem. Phys.*, 2007, **126**, 014101.
- 12 S. Nosé, M. L. Klein, *Mol. Phys.*, 1983, **50**, 1055.
- 13 E. F. Pettersen, T. D. Goddard, C. C. Huang, E. C. Meng, G. S. Couch, T. I. Croll, J. H. Morris, T. E. Ferrin, *Protein Sci.*, 2021, **30**, 70.
- 14 X. Zhang, J. Li, Y. Liu, B. Lu, S. Liang, J. Zhou, *Nat. Commun.*, 2024, **15**, 22735.
- 15 J. Duan, J. Dong, R. Cao, H. Yang, K. Fang, Y. Liu, Z. Shen, F. Li, R. Liu, H. Li, C. Chen, *Adv. Sci.*, 2023, **10**, 2303343.
- 16 H. Lu, J. Hu, X. Wei, K. Zhang, X. Xiao, J. Zhao, Q. Hu, J. Yu, G. Zhou, B. Xu, *Nat. Commun.*, 2023, **14**, 4435.
- 17 Y. Gao, N. Yang, F. Bu, Q. Cao, J. Pu, Y. Wang, T. Meng, J. Chen, W. Zhao, C. Guan, *Energy Environ. Sci.*, 2024, **17**, 1894.
- 18 N. Yang, Y. Gao, F. Bu, Q. Cao, J. Yang, J. Cui, Y. Wang, J. Chen, X. Liu, C. Guan, *Adv. Mater.*, 2024, DOI: 10.1002/adma.202312934, 2312934.
- 19 Y. Zeng, Z. Pei, Y. Guo, D. Luan, X. Gu, X. W. Lou, *Angew. Chem. Int. Ed.*, 2023,

- 62**, e202312145.
- 20 H. Dong, X. Hu, R. Liu, M. Ouyang, H. He, T. Wang, X. Gao, Y. Dai, W. Zhang, Y. Liu, Y. Zhou, D. J. L. Brett, I. P. Parkin, P. R. Shearing, G. He, *Angew. Chem. Int. Ed.*, 2023, **62**, e202311268.
 - 21 H. Peng, C. Wang, D. Wang, X. Song, C. Zhang, J. Yang, *Angew. Chem. Int. Ed.*, 2023, **62**, e202308068.
 - 22 H. Wang, W. Ye, B. Yin, K. Wang, M. S. Riaz, B. B. Xie, Y. Zhong, Y. Hu, *Angew. Chem. Int. Ed.*, 2023, **62**, e202218872.
 - 23 K. Zhou, G. Liu, X. Yu, Z. Li, Y. Wang, *J. Am. Chem. Soc.*, 2024, **146**, 9455.
 - 24 Q. He, Y. Zhong, J. Li, S. Chai, Y. Yang, S. Liang, Z. Chang, G. Fang, A. Pan, *Adv. Energy Mater.*, 2024, DOI: 10.1002/aenm.202400170, 2400170.
 - 25 W. Zhang, F. Guo, H. Mi, Z. Wu, C. Ji, C. Yang, J. Qiu, *Adv. Energy Mater.*, 2022, **12**, 2202219.
 - 26 Y. Cheng, Y. Jiao, P. Wu, *Energy Environ. Sci.*, 2023, **16**, 4561.
 - 27 Q. Liu, Z. Yu, Q. Zhuang, J. K. Kim, F. Kang, B. Zhang, *Adv. Mater.*, 2023, **35**, 2300498.
 - 28 Y. Qin, H. Li, C. Han, F. Mo, X. Wang, *Adv. Mater.*, 2022, **34**, 2207118.
 - 29 X. Yang, Z. Zhang, M. Wu, Z. Guo, Z. Zheng, *Adv. Mater.*, 2023, **35**, 2303550.
 - 30 G. Li, Z. Zhao, S. Zhang, L. Sun, M. Li, J. A. Yuwono, J. Mao, J. Hao, J. Vongsvivut, L. Xing, C. Zhao, Z. Guo, *Nat. Commun.* 2023, **14**, 6526.